Journal of Catalysis 418 (2023) 190–202

Contents lists available at ScienceDirect

Journal of Catalysis

journal homepage: www.elsevier.com/locate/jcat

# Adsorption, surface reactions and hydrodeoxygenation of acetic acid on platinum and nickel catalysts

Lotanna Ezeonu [a], Ziyu Tang [a], Yue Qi [a], Fangliang Huo [a], Yiteng Zheng [a,b], Bruce E. Koel [b,*], Simon G. Podkolzin [a,*]

[a] Department of Chemical Engineering and Materials Science, Stevens Institute of Technology, Hoboken, NJ 07030, United States
[b] Department of Chemical and Biological Engineering, Princeton University, Princeton, NJ 08544, United States

ARTICLE INFO

*Article history:*
Received 21 August 2022
Revised 13 January 2023
Accepted 14 January 2023
Available online 18 January 2023

ABSTRACT

Acetic acid adsorption and surface reactions were studied on Pt(111) and Ni(110) with infrared reflection–absorption spectroscopy (IRAS) and temperature programmed desorption as well as computationally on the same well-defined single-crystal surfaces with density functional theory calculations. Additional calculations were performed for Ni(111) for comparison with Pt(111). At high acetic acid exposures at the dosing temperature of 90 K, acetic acid forms a chemisorbed layer covered by a physisorbed multilayer. The chemisorbed layer at 90 K for both Pt and Ni contains a mixture of molecularly adsorbed acetic acid as well as acetate. The physisorbed multilayer desorbs at 157–172 K. At 200 K, while a mixture of molecular acetic acid and acetate remains on Pt(111), acetic acid almost completely decomposes into acetate and, furthermore, produces some CO on Ni(110). Due to the almost complete decomposition of acetic acid on Ni at 200 K, only a small fraction of the chemisorbed acetic acid desorbs molecularly at 220 K. Unlike on Ni(110), most of the chemisorbed acetic acid desorbs molecularly from Pt(111) at a similar temperature of 218 K. Recombinative desorption of acetic acid is observed as a broad peak at 345 K for Pt(111) and as a tail peak at 220–300 K for Ni(110). At 450 K, the decomposition of acetic acid is almost complete on both metals. In contrast with acetic acid surface reactions where Ni is equally or even more reactive than Pt, a 1.5 wt % $Ni/SiO_2$ catalyst is less active than a 5 wt % $Pt/SiO_2$ catalyst in vapor-phase acetic acid hydrodeoxygenation at 473 and 573 K. Hydrogen temperature programmed reduction measurements for calcined catalysts show that Ni requires a higher temperature of 622 K for its reduction than 564 K for Pt. Therefore, the lower catalytic activity of Ni in hydrodeoxygenation can be attributed to the lower reducibility of Ni and not the differences in acetic acid adsorption or surface reactions.



## 1. Introduction

Pt and Ni catalysts are actively studied and often used as benchmarks in the development of improved technologies for the conversion of biomass-derived feedstocks into fuels and chemical intermediates, specifically for hydrodeoxygenation and steam reforming of bio-oils [1–5]. Since acetic acid is a component of bio-oils as well as a widely used model compound, it is important to better understand its adsorption and reactivity on Pt and Ni catalytic surfaces at the molecular level [3–7]. In this work, adsorption and surface chemistry of acetic acid on single-crystals of Pt and Ni were studied experimentally with infrared reflection–absorption spectroscopy (IRAS) and temperature programmed desorption (TPD) as well as computationally on the same well-defined metal surfaces with density functional theory (DFT) calculations. In addition, silica-supported Pt and Ni catalysts were compared in vapor-phase acetic acid hydrodeoxygenation in a fixed-bed flow reactor as well as characterized with transmission electron microscopy (TEM), hydrogen temperature programmed desorption ($H_2$ TPD) and hydrogen temperature programmed reduction ($H_2$ TPR) measurements.

For Pt, acetic acid adsorption and reactions as a function of surface coverage and temperature were previously studied on Pt(111) with electron energy loss spectroscopy (EELS) [8], high resolution electron energy loss spectroscopy (HREELS) combined with TPD [9,10] and synchrotron radiation photoelectron spectroscopy (SRPES) combined with TPD [11] as well as on $Pt/SiO_2$ and $Pt/TiO_2$ with diffuse reflectance infrared Fourier transform

* Corresponding authors.
*E-mail addresses:* bkoel@princeton.edu (B.E. Koel), Simon.Podkolzin@Stevens.edu (S.G. Podkolzin).

https://doi.org/10.1016/j.jcat.2023.01.013
0021-9517/

spectroscopy (DRIFTS) combined with TPD [12]. In those spectroscopic studies, there were some uncertainties and disagreements in the hydrocarbon surface species proposed based on the experimental vibrational frequencies. In this work, experimental IRAS and TPD measurements were combined with DFT geometry optimization and frequency calculations for the determination of the structure, energetic stability and vibrational frequencies of the hydrocarbon surface species on Pt(111). Our previous study with IRAS and TPD measurements combined with DFT calculations did the same for Ni(110) [13]. For a better comparison between Pt and Ni, additional DFT calculations were performed in this work on Ni(111) to match the calculations on Pt(111) in terms of the metal crystal plane, hydrocarbon surface coverage and computational settings.

In addition to obtaining an improved understanding of acetic acid adsorption and surface reactions, it is useful to compare Pt and Ni at the same reaction conditions and explain why Ni catalysts are typically less active than Pt catalysts in acetic acid hydrodeoxygenation. It was previously proposed that the rate determining step for acetic acid decomposition on Pt and Ni might be different or, if the rate determining step was the same, its activation energy on Pt might be lower or, perhaps, that the hydrogen-assisted C-O bond breaking might be more efficient on Pt than on Ni. In contradiction with those proposed explanations, our previous study showed that Ni catalyzes decomposition of adsorbed acetic acid in surface science experiments at temperatures well below typical hydrodeoxygenation reaction temperatures [13]. Therefore, the overall hydrodeoxygenation activity is unlikely to be limited by the hydrocarbon surface reactions on Ni. Instead, it is more likely to be limited by the reducibility of the Ni surface. Acetic acid decomposition can proceed efficiently on Ni only once, as in surface science experiments, if surface oxygen produced in the decomposition cannot be easily removed with gas-phase $H_2$ under the reaction conditions to regenerate the metal surface and, thus, complete the catalytic cycle. In this work, this alternative explanation was evaluated by performing acetic acid hydrodeoxygenation reaction testing with reduced Pt and Ni catalysts and $H_2$ TPR measurements with oxidized Pt and Ni catalysts.

## 2. Methods

### 2.1. Catalyst preparation

5 wt % $Pt/SiO_2$ and 1.5 wt % $Ni/SiO_2$ catalysts (equivalent molar metal loadings) were prepared with an incipient wetness impregnation method using tetraammineplatinum(II) nitrate, $Pt(NH_3)_4(NO_3)_2$ (Sigma-Aldrich, 99.995% trace metals basis), and nickel(II) nitrate hexahydrate, $Ni(NO_3)_2{\cdot}6H_2O$ (Sigma-Aldrich, 99.999% trace metals basis). Prior to metal deposition, the $SiO_2$ support (Cabot CAB-O-SIL HS-5 fumed silica) was dried by increasing the temperature at 1 K/min to 393 K and holding at this temperature for 2 h. After drying, the $SiO_2$ support was calcined by increasing the temperature at 5 K/min to 723 K and holding for 2 h. After metal deposition, the samples were dried by increasing the temperature at 1 K/min to 323 K and holding for 4 h followed by increasing the temperature at 1 K/min to 393 K and holding for 2 h. Afterwards, the samples were calcined in static air by increasing the temperature at 5 K/min to 723 K and holding for 2 h. The same 5 wt % $Pt/SiO_2$ catalyst was used in our previous studies on acetic acid hydrodeoxygenation over Pt and Pt-Mo [4,5]. The same 1.5 wt % $Ni/SiO_2$ catalyst was used in our previous study on propylene adsorption and propane dehydrogenation to propylene over Ni and Ni-Sn [14]. Similar synthesis methods were previously used for the preparation of other supported metal catalysts [15–21].

Prior to TEM measurements, the calcined catalyst samples were reduced in a Micromeritics AutoChem HP 2950 reactor system equipped with a furnace, three mass flow controllers and a thermal conductivity detector (TCD). The reactor system with a catalyst was first purged with an Ar (Praxair, ultrahigh purity 99.999%) flow for 30 min. The catalysts were then dried in a flow of 20 mol % $H_2$ (Praxair, ultrahigh purity, 99.999%) in Ar by increasing the temperature at 1 K/min to 383 K and holding for 1 h. After drying, the catalysts were reduced by increasing the temperature at 5 K/min to 573 K with a 4-h hold for Pt and to a higher temperature of 723 K with a shorter 2-h hold for Ni. After reduction, the catalysts were cooled to 303 K in an Ar flow. TEM images were obtained with a FEI Titan Themis 200 instrument at an acceleration voltage of 200 kV. Representative TEM images are shown in Fig. 1. The average metal particle sizes of 3 nm for Pt and 20 nm for Ni were determined by analyzing multiple TEM images with ImageJ 1.52 software by the National Institutes of Health. These metal particle sizes are consistent with the metal dispersion values of 34% for Pt and 26% for Ni obtained with the $H_2$ TPD measurements described below.

### 2.2. Catalyst characterization with $H_2$ TPD and $H_2$ TPR

The metal dispersion values for the 5 wt % $Pt/SiO_2$ and 1.5 wt % $Ni/SiO_2$ catalysts were evaluated with $H_2$ TPD using the same Micromeritics AutoChem HP 2950 reactor flow system, which was used for catalyst reduction prior to the TEM measurements. In a TPD experiment, about 0.15 g of a calcined sample was loaded into a U-shaped quartz reactor and secured with quartz wool (Altamira Instruments, Inc.). The reduction procedure was the same as that prior to the TEM measurements. First, the reactor system with the sample was purged with a 50 sccm Ar flow for 30 min. The gas flow was then switched to 20% $H_2$/Ar with the same total flow rate, and the temperature was increased at 1 K/min to 383 K and held for 1 h. Afterwards, the temperature was increased at 5 K/min to 573 K with a 4-h hold for Pt and to 723 K with a 2-h hold for Ni. Finally, the temperature was lowered to 303 K in the same flow of 20% $H_2$/Ar for $H_2$ adsorption. Subsequently, the flow was switched to 50 sccm Ar for at least 30 min to remove physisorbed $H_2$, purge the system and obtain a stable TCD baseline for 10 min. Desorption was performed by increasing the temperature at 10 K/min to 573 K when all $H_2$ desorbed. The metal dispersion values were calculated using the integral area of the TCD $H_2$ desorption peak, assuming the adsorbed H to surface metal atomic ratio of unity.

$H_2$ TPR measurements were performed similarly to the $H_2$ TPD measurements using the same Micromeritics AutoChem HP 2950 reactor flow system, except calcined catalysts were used without a reduction pretreatment. In a TPR experiment, about 0.15 g of a calcined sample was loaded into a U-shaped quartz reactor and secured with quartz wool. A 50 sccm Ar flow for 30 min was used to purge the system. The flow was then switched to 20 mol % $H_2$/Ar

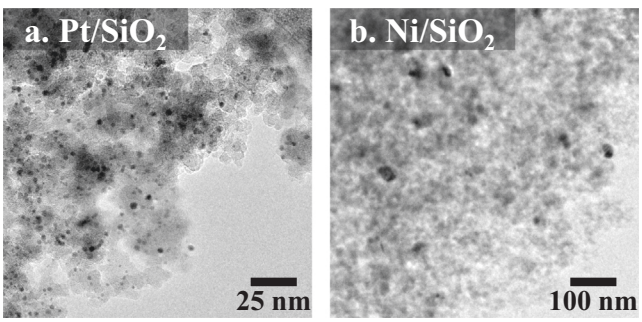


**Fig. 1.** TEM images of (a) 5 wt % $Pt/SiO_2$ and (b) 1.5 wt % $Ni/SiO_2$.

with the same total flow rate. After a stable baseline was observed for 10 min, the temperature was increased at 10 K/min, and the effluent was analyzed for water formation using a Hiden Analytical HPR 20 mass spectrometer by monitoring the mass-to-charge ratio ($m/z$) of 18.

### 2.3. Acetic acid hydrodeoxygenation reaction testing

Reaction testing was performed in vapor phase in a fixed-bed flow reactor previously used for acetic acid hydrodeoxygenation over Pt and Pt-Mo catalysts [4,5] and for selective ethanol oxidation over zeolite-supported Au catalysts [15]. In each test, about 0.1 g of an undiluted fresh catalyst sample was loaded into a 316 stainless steel tubular reactor with a 0.25-in outside diameter, 0.18-in inside diameter and 2.5-in length. Each end of the reactor was fitted with a metal cloth filter (200 × 1150 mesh, Hastelloy C Filter Cloth). The reactor was placed inside a Mellen Microtherm MTSC 12.5R-3X6-1Z vertical-split tube furnace equipped with three temperature zones for accurate temperature monitoring and control (Omega CN7800 temperature controller). Gas flows of $N_2$ (Praxair, ultrahigh purity, 99.999%) and $H_2$ were controlled with Bronkhorst EL-Flow Select mass flow controllers. The reactor outlet pressure was atmospheric.

Prior to reaction testing, the catalysts were dried and reduced in situ at 573 K for Pt and 723 K for Ni using the same procedure used prior to the TEM and $H_2$ TPD measurements. After reduction, the temperature was decreased to the reaction testing temperature under a 50 sccm $N_2$ flow. During reaction testing, a gas feed of 40 mol % $H_2/N_2$ with a total flow rate of 100 sccm was used. After the temperature stabilized at a desired value, a flow of liquid acetic acid, $CH_3COOH$ (Sigma-Aldrich, Reagent Plus, >99%), was started at 0.03 mL/min and mixed with the gas flow as vapor in a T-joint (Swagelok) preheater kept at 423 K. All reactants (11 kPa acetic acid and 36 kPa $H_2$ in $N_2$) were fed into the preheater through separate check valves to prevent backflow. The acetic acid flow rate was controlled by a Scientific System Series III high-performance liquid chromatography (HPLC) pump. The moment of acetic acid introduction was taken as the start of the time on stream.

The feed flow rate was chosen to limit acetic acid conversion to values below 7% for both Pt and Ni catalysts at all testing conditions so that a differential reactor model could be used in the analysis of the kinetic measurements. Similar to our previous reaction rate measurements for acetic acid hydrodeoxygenation over Pt and Pt-Mo catalysts [4,5], acetic acid reaction rates are reported as turnover frequency (TOF) values for stabilized activity after 2 h of time on stream. In this study, the reaction rates are reported as an average of values obtained between 2 and 4 h of time on stream. The confidence interval for each reported rate measurement was obtained based on at least three independent runs, each with a fresh catalyst sample. The TOF values (moles of acetic acid per mole of surface metal per second) were calculated using the metal dispersion values of 34% for Pt and 26% for Ni obtained with the $H_2$ TPD measurements. In addition, the reaction rates are also provided without adjusting for the metal dispersion as moles of acetic acid per gram of catalyst per second ($mol_{CH3COOH}/(g_{catalyst}\ s)$) and as moles of acetic acid per mole of total metal per second ($mol_{CH3COOH}/(mol_{metal}\ s)$).

Reaction products were analyzed with online sampling using a Varian-450 gas chromatograph (GC) equipped with three columns, three rotary valves (VICI AG International) and a split/splitless injector. The sampling line from the reactor to the GC was heat traced and kept at 423 K (rope heater Omega FGR100, solid state relay Omega SSLR240DC10 and PID controller Omega CN7823). A GC analysis began by filling two 1/16-in stainless steel sample loops (Valco Sample Loop 250 and 1000 μL). The sample from the 250-μL loop was separated using a HayeSep Q 80/100 (6 ft × 1/16 in) column and a Molecular Sieve 5A 60/80 (4 ft × 1/16 in) column and analyzed for concentrations of $H_2$, $N_2$, CO and $CO_2$ with a TCD using Ar as the carrier and reference gas. The valve timing and rotation were set in such a way that $CO_2$ was not fed to the Molecular Sieve 5A column. The sample from the 1000-μL loop was separated using a CP8690 capillary column (CP-Sil 5CB, 5 μm, 60 m × 0.32 mm) and analyzed for determining concentrations of all hydrocarbons with a flame ionization detector (FID) using He as the carrier gas and a $H_2$ flow for the flame. The TCD was calibrated with reference mixtures of gases in Ar. The FID was calibrated with reference mixtures of acetic acid and its reaction products. Reaction selectivities are reported for carbon-containing products.

The same equipment and procedures were used previously for studying acetic acid hydrodeoxygenation over Pt and Pt-Mo catalysts [4,5].

### 2.4. TPD and IRAS of acetic acid on Pt(111) and Ni(110)

The Pt(111) and Ni(110) crystals (8 mm square, ±0.5° orientation) were cleaned by sputtering with 1.5 keV $Ar^+$ ions and annealing at 1100 K. To eliminate residual carbon, the surface was annealed in oxygen, $P(O_2) = 4 \times 10^{-8}$ Torr, at 1000 K. Hydrogen treatments at $P(H_2) = 4 \times 10^{-8}$ Torr at 1000 K were used to eliminate residual oxygen. The surface cleanliness was checked with Auger electron spectroscopy (AES), and the surface order and periodicity were verified with the low-energy electron diffraction (LEED) patterns.

TPD experiments were performed in a three-level stainless steel ultrahigh-vacuum (UHV) chamber ($2 \times 10^{-10}$ Torr base pressure) with the sample in the line of sight of the ionizer of a shielded UTI 100C quadrupole mass spectrometer. The shield nozzle was 1 mm from the sample. The heating rate was 3 K/s. Custom software enabled monitoring of up to eight masses simultaneously.

IRAS experiments were performed in a separate UHV chamber using a Bruker Vertex 70 instrument with a grazing incidence of 75° from the surface normal and a mercury–cadmium–telluride detector cooled with liquid nitrogen. Spectra were obtained with a resolution of 2 $cm^{-1}$ by averaging 512 scans over 5 min by first dosing acetic acid at 90 K, annealing to a desired temperature and then cooling back to 90 K for spectra collection. Glacial acetic acid (Sigma-Aldrich, ≥99.99%) was degassed through freeze–pump–thaw cycles and dosed via a variable precision leak valve. Since acetic acid decomposition resulted in the formation of residual carbon on the surface, the crystals were annealed in oxygen and then in vacuum at 1100 K to remove residual carbon from the surface before each TPD and IRAS experiment. The same equipment and experimental procedures were used previously for studying acetic acid adsorption and reactions on Ni(110) [13].

### 2.5. Computational methods

Gradient-corrected spin-polarized periodic DFT calculations with the DMol$^3$ code in Materials Studio 2017 by Dassault Systèmes BIOVIA Corporation were performed for determining geometries and adsorption energies of molecularly adsorbed acetic acid and its reaction products on infinite Pt(111) and Ni(111) surfaces constructed by using periodic unit cells. In addition, vibrational frequencies for acetic acid, acetate and acetyl adsorbed on Pt(111) were calculated for interpretation of the experimental IRAS spectra. Each unit cell had 3×3 surface metal atoms with 5 layers for a total of 3×3×5 = 45 metal atoms. The unit cells with molecularly adsorbed acetic acid are shown in Fig. 2. The surface coverage was 1/9 ML: one acetic acid molecule on the surface with 3×3 metal atoms. The unit cells were generated from the corresponding bulk crystal using the optimized lattice constants of 0.3995 nm for Pt (within 1.8% of the 0.3924 nm experimental value) and

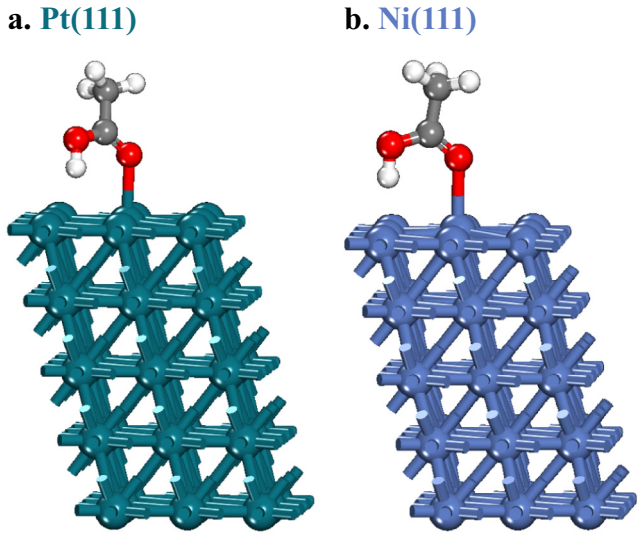


**Fig. 2.** Molecular acetic acid adsorbed on 3×3×5 periodic unit cells used to construct infinite surfaces of (a) Pt(111) and (b) Ni(111) for density functional theory calculations.

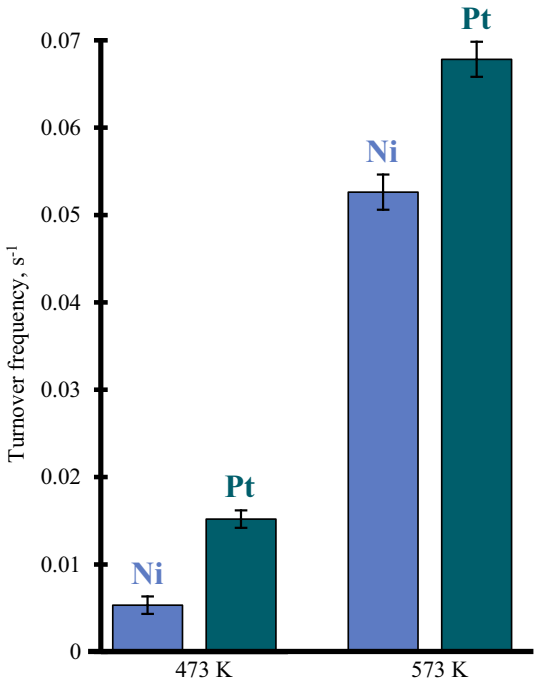


**Fig. 3.** Acetic acid reaction rates for 5 wt % $Pt/SiO_2$ and 1.5 wt % $Ni/SiO_2$ for gas-phase hydrodeoxygenation in a fixed-bed flow reactor at 11 kPa acetic acid and 36 kPa hydrogen (balance nitrogen) at atmospheric pressure.

0.3541 nm for Ni (within 0.5% of the 0.3524 nm experimental value). A vacuum spacing of 4 nm in the *c* direction was used. The top three layers of the surfaces were optimized with adsorbates during geometry optimizations, simulating surface relaxation after adsorption. The remaining two bottom layers were constrained at the bulk crystal positions, simulating the bulk structure.

The calculations used the double numerical with polarization (DNP) basis set and the generalized gradient-corrected Perdew–Wang (GGA PW91) functional. Tightly bound core electrons of Pt and Ni were represented with semicore pseudopotentials. Reciprocal-space integration over the Brillouin zone was approximated through k-point sampling with a separation of 0.4 $nm^{-1}$ using the Monkhorst-Pack grids of 3×3×1 for Pt and 4×4×1 for Ni. A value of 0.08 for both charge and spin density mixing with direct inversion in the iterative subspace (DIIS) and orbital occupancy with thermal smearing of 0.002 Ha were used. The formal spin for the Ni atoms was initially set to +2 to improve convergence. The orbital cutoff distance of 0.4 nm was set for all atoms. Similarly constructed periodic surfaces with similar computational settings were previously used successfully for studying adsorption and reactions on other metal surfaces. [17,21–29].

Adsorption energies were calculated at 0 K without zero-point energy corrections using as a reference the sum of energies for the corresponding metal surface and an isolated acetic acid molecule calculated separately. Adsorption energies are reported as positive numbers, $-\Delta E_{ads}$. Frequency calculations were performed using a partial Hessian matrix for adsorbed hydrocarbon structures. All vibrational frequencies for all adsorbed hydrocarbon structures on Pt(111) were scaled by a single factor of 1.0524, which was obtained by matching the experimental frequency of 1425 $cm^{-1}$ to the $\nu_s$(OCO) vibration of the bridge-bonded acetate bidentate structure on this Pt surface. For comparison, the frequency scaling factor for Ni(110) in our previous study was 1.0235, which was similarly obtained by matching the experimental frequency of 1429 $cm^{-1}$ to the $\nu_s$(OCO) vibration of the bridge-bonded acetate bidentate structure on this Ni surface [13].

## 3. Results

### 3.1. Acetic acid hydrodeoxygenation over $Pt/SiO_2$ and $Ni/SiO_2$

At 473 K, acetic acid reaction rates were 0.015 ± 0.001 1/s (1.5% conversion, 1.3 ± 0.1 × $10^{-6}$ $mol_{CH3COOH}/(g_{catalyst}$ s), 0.0052 ± 0.00 05 $mol_{CH3COOH}/(mol_{metal}$ s)) for 5 wt % $Pt/SiO_2$ and 0.005 ± 0.001 1/s (0.4% conversion, 0.35 ± 0.05 × $10^{-6}$ $mol_{CH3COOH}/(g_{catalyst}$ s), 0.0014 ± 0.0002 $mol_{CH3COOH}/(mol_{metal}$ s)) for 1.5 wt % $Ni/SiO_2$. At 573 K, the reaction rates increased to 0.067 ± 0.002 1/s (6.7% conversion, 5.9 ± 0.2 × $10^{-6}$ $mol_{CH3COOH}/(g_{catalyst}$ s), 0.0229 ± 0.0008 $mol_{CH3COOH}/(mol_{metal}$ s)) for Pt and 0.052 ± 0.002 1/s (4.0% conversion, 3.5 ± 0.2 × $10^{-6}$ $mol_{CH3COOH}/(g_{catalyst}$ s), 0.0136 ± 0.0006 $mol_{CH3COOH}/(mol_{metal}$ s)) for Ni (Fig. 3). Product selectivities are summarized in Table 1. At 473 K, the main products for Pt were undesirable $C_1$ products: carbon monoxide (CO) and methane ($CH_4$) accounted for 82%. The largest desirable $C_2$ product was ethane ($C_2H_6$) at 11%. The second largest $C_2$ product was ethanol ($C_2H_5OH$) at 5%. The amount of acetaldehyde ($CH_3CHO$) was small, 1%. In contrast with Pt, Ni was less active but more selective to $C_2$ products at this temperature. Carbon monoxide was not observed, and $C_1$ hydrocarbons, methane and methanol ($CH_3OH$), accounted for 34%, while $C_2$ hydrocarbons accounted for 36%. In addition, a $C_4$ hydrocarbon ethyl acetate ($CH_3COOC_2H_5$) accounted for 30% for Ni, whereas it was only 1% for Pt. At a higher temperature of 573 K, both catalysts were less selective to $C_2$ products. Only 9% ethanol was observed for Pt, while acetaldehyde, ethanol and ethane were each 1% for a total of only 3% for Ni. The $C_2$ selectivity decrease was, thus, more significant for Ni. The undesirable $C_1$ products, correspondingly, increased and accounted for 91% for both catalysts. Ethyl acetate decreased to 6% for Ni, and it was no longer detected for Pt.

**Table 1**
Selectivities for carbon-containing products in acetic acid hydrodeoxygenation at 11 kPa acetic acid and 36 kPa hydrogen for 5 wt % $Pt/SiO_2$ and 1.5 wt % $Ni/SiO_2$, mol %.

| | 473 K | | 573 K | |
|---|---|---|---|---|
| | Pt | Ni | Pt | Ni |
| *Conversion, %* | *1.5* | *0.4* | *6.7* | *4.0* |
| CO | 41 | 0 | 45 | 39 |
| $CH_4$ | 41 | 29 | 46 | 52 |
| $CH_3OH$ | 0 | 5 | 0 | 0 |
| $C_2H_6$ | 11 | 24 | 9 | 1 |
| $CH_3CHO$ | 1 | 5 | 0 | 1 |
| $C_2H_5OH$ | 5 | 7 | 0 | 1 |
| $CH_3COOC_2H_5$ | 1 | 30 | 0 | 6 |

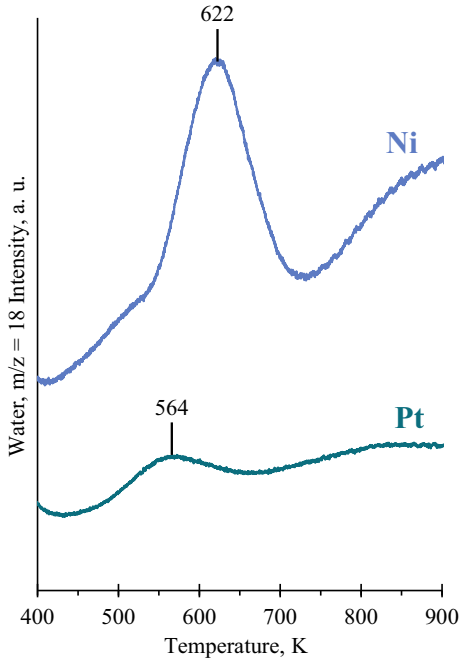


**Fig. 4.** Hydrogen temperature programmed reduction curves for 5 wt % $Pt/SiO_2$ and 1.5 wt % $Ni/SiO_2$ catalysts.

### 3.2. TPR of $Pt/SiO_2$ and $Ni/SiO_2$

In $H_2$ TPR measurements, a calcined 5 wt % $Pt/SiO_2$ sample produced a small broad peak for water at about 564 K. In contrast, a calcined 1.5 wt % $Ni/SiO_2$ sample produced a more well-defined bigger peak at a higher temperature of 622 K (Fig. 4).

### 3.3. IRAS of acetic acid on Pt(111) and Ni(110)

The IRAS spectra after dosing acetic acid at 90 K and then annealing to multiple higher temperatures are shown in Fig. 5. For Pt, at the dosing temperature of 90 K, the following peaks were observed: 968, 1049, 1304, 1364, 1412, 1435, 1676, 1730, 2930 and 2987 $cm^{-1}$. At higher temperatures, fewer peaks with lower intensities were observed. At 193 K, only peaks at 968, 1049, 1406, 1425 and 1676 $cm^{-1}$ were observed. A new small peak appeared at 1703 $cm^{-1}$. At 250 K, the intensity of the peak at 1406 $cm^{-1}$ decreased, and the peak at 1425 $cm^{-1}$ was no longer observed. Instead, new peaks appeared at 1595 and 2085 $cm^{-1}$. Moreover, the peak at 968 $cm^{-1}$ was no longer observed and, instead, a smaller 974 $cm^{-1}$ peak at a neighboring position appeared. This new peak remained practically unchanged at higher temperatures. At 440 K, the intensity of the 2085 $cm^{-1}$ peak increased further, and two new peaks at 1878 and 2062 $cm^{-1}$ appeared. The peaks at 1406 and 1595 $cm^{-1}$ were no longer observed. At the highest tested temperature of 770 K, only two peaks remained: the mostly unchanged peak at 974 $cm^{-1}$ and a small peak at 2085 $cm^{-1}$.

IRAS measurements for Ni after initial acetic acid coverage values of 0.18 and 2.9 ML as a function of annealing temperature were reported previously [13]. In that previous study, acetic acid exposure values in Langmuir units (L) were converted into monolayer (ML) units. In this work, the measurements at 2.9 ML (0.14 L) are included in Fig. 5b for comparison with the measurements for Pt at a similar exposure of 0.15 L in Fig. 5a. An additional spectrum for Ni at 450 K, which was not reported previously, is included for comparison with the spectrum for Pt at a similar temperature of 440 K. At the dosing temperature of 90 K, the following peaks were observed for Ni: 964, 1055, 1311, 1421, 1456, 1628, 1690, 1730, 2931 and 2989 $cm^{-1}$. Similarly to Pt, fewer peaks were observed at higher temperatures for Ni. At 200 K, only peaks at 1055, 1421, 1456, 1628, 1690 and 2931 $cm^{-1}$ remained, plus a new peak at 1832 $cm^{-1}$ appeared. At 350 K, the peaks at 1055, 1421, 1456 and 2931 $cm^{-1}$ remained. The 1456 $cm^{-1}$ peak increased in intensity. Instead of a small peak at 1832 $cm^{-1}$, two similarly small peaks at 1876 and 2010 $cm^{-1}$ appeared. At 450 K, only three peaks were observed: the intensity of the 1456 $cm^{-1}$ peak decreased significantly, a small peak remained at 1055 $cm^{-1}$, and a new peak at 974 $cm^{-1}$ appeared.

### 3.4. TPD of acetic acid from Pt(111) and Ni(110)

The TPD curves for 60 amu, the parent mass of acetic acid, after acetic acid adsorption on Pt(111) and Ni(110) at multiple exposures at 90 K are compared in Fig. 6. For Pt, at the lowest exposure of 0.01 L, a small broad peak was observed at about 218 K (Fig. 6a). At a higher exposure of 0.02 L, this broad peak became more well-defined, and a new smaller peak at 166 K appeared. At higher exposures of 0.04–0.08 L, the intensities of these two peaks increased, with the peak at 215–218 K remaining dominant. At the highest used exposure of 0.08 L, an additional peak appeared at about 345 K. This third peak was small and broad.

For Ni, at the lowest exposure of 0.02 L, a small broad peak at about 220 K was observed (Fig. 6b). At 0.04 L, this peak increased but remained broad with a tail extending to 300 K. In addition, a new peak at 157 K appeared. At higher exposures of 0.06–0.08 L, the intensities of these two peaks increased, and a smaller shoulder feature was observed at 175 K. Unlike for Pt, there was no additional peak above 300 K. The TPD results for Ni in this study have acetic acid exposure values similar to those for Pt. Our TPD results for Ni in a wider range of exposures, which correspond to acetic acid coverage values from 0.12 to 7.3 ML, were reported previously [13].

The acetic acid TPD curves at a single acetic acid exposure – 0.08 L for Pt and 0.14 L for Ni – are compared to the TPD curves of accompanying decomposition products $H_2$ (2 amu), $H_2O$ (18

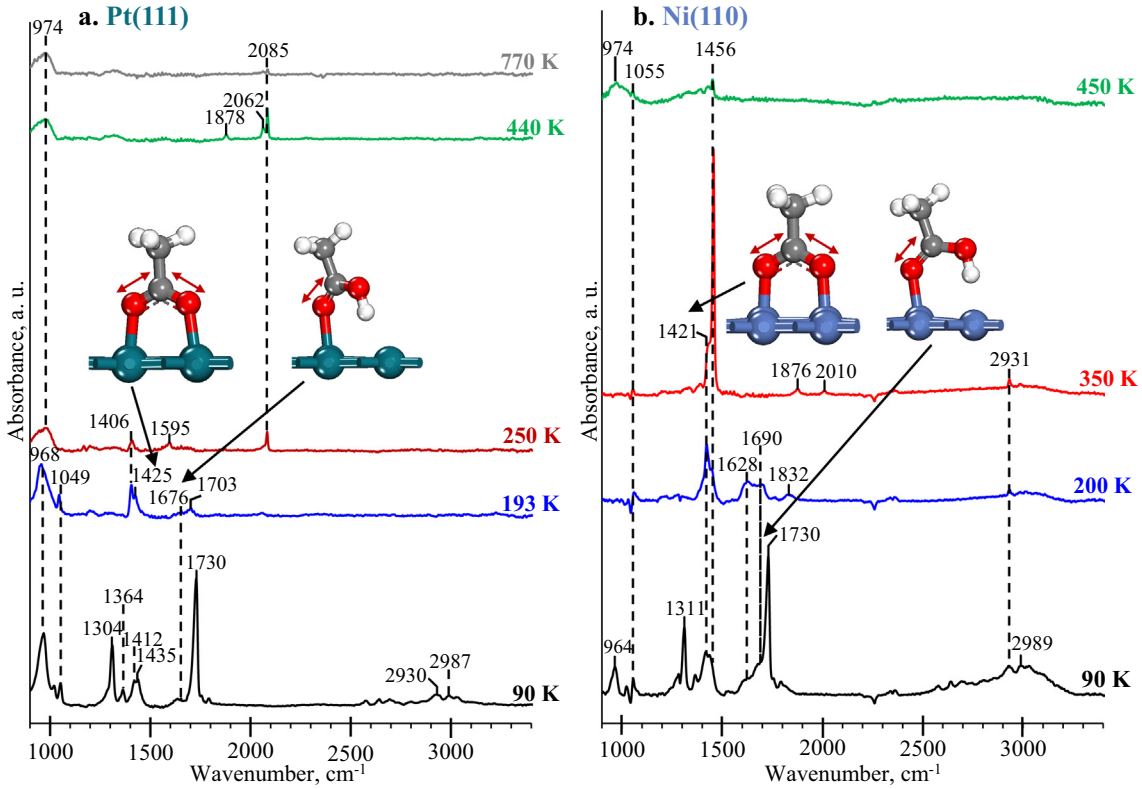


**Fig. 5.** IRAS spectra as a function of annealing temperature for acetic acid on (a) Pt(111) after exposure of 0.15 L and (b) Ni(110) after exposure of 0.14 L.

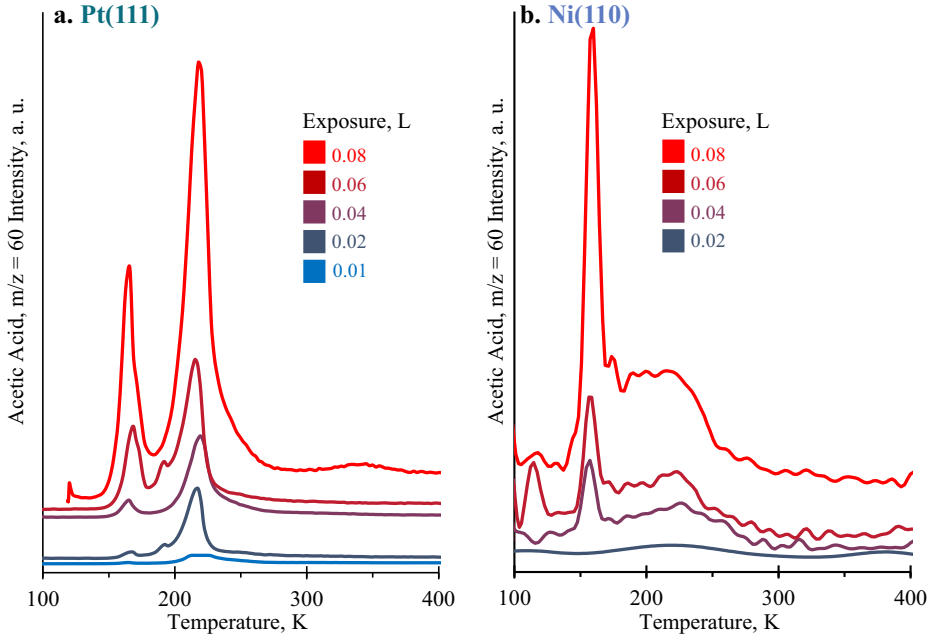


**Fig. 6.** Acetic acid ($m/z$ = 60) TPD curves for (a) Pt(111) and (b) Ni(110) after multiple exposures at 90 K.

amu), CO (28 amu) and $CO_2$ (44 amu) in Fig. 7. The CO curves were not corrected for the $CO^+$ cracking product from $CO_2$. For Pt, the acetic acid desorption peaks are larger than the peaks for each of the monitored decomposition products (Fig. 7a). For Ni, in contrast, the acetic acid desorption peaks are smaller than the peaks of each of the monitored decomposition products, except $H_2O$ (Fig. 7b). For Pt, $H_2$ desorption was observed first at 357 K and then as a small peak at a higher temperature of 451 K. No identifiable peaks were detected for $H_2O$. A small $CO_2$ peak at 388 K was followed by a larger CO peak at 444 K. For Ni, $H_2$ desorption was observed first at 265 K and then as a larger peak at a higher temperature of 425 K. This second $H_2$ peak coincided with CO and $CO_2$ desorption. A small $H_2O$ peak was observed at a lower temperature of 310 K.

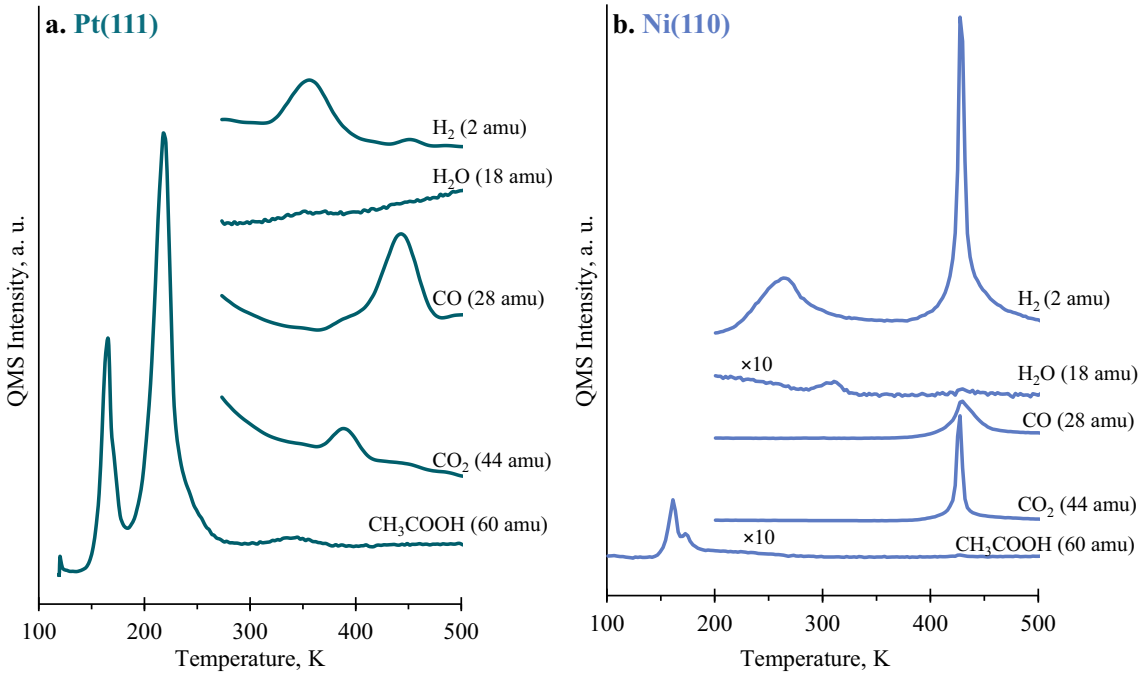


**Fig. 7.** TPD curves for acetic acid and its decomposition products for (a) Pt(111) after 0.08 L exposure at 90 K and (b) Ni(110) after 0.14 L exposure at 100 K.

### 3.5. DFT calculations

The calculated vibrational frequencies for an isolated acetic acid molecule are listed in Table 2 with our assignments made based on visualization of the vibrational modes. Experimental peaks observed with infrared (IR) spectroscopy for acetic acid monomer in the gas phase reported in our previous study [13] and in an earlier publication by the U.S. National Bureau of Standards [30] are included in Table 2 for comparison.

The vibrational assignments made for acetic acid monomer were extended to the interpretation of acetic acid in a physisorbed multilayer, which is expected to form above a chemisorbed monolayer at the dosing temperature of 90 K at the acetic acid exposure values employed for collecting the IRAS spectra in Fig. 5. The IRAS peaks at 90 K that are consistent with such a physisorbed multilayer for both Pt and Ni are listed in Table 3. For comparison, Table 3 includes experimental IR peaks for acetic acid in other condensed states: gas phase at 298 K reported in our previous study [13] as well as liquid and solid reported in earlier publications [33,34].

**Table 2**
Calculated vibrational frequencies and experimental IR peaks for acetic acid monomer, $cm^{-1}$.

| Vibration[a] | Calculated monomer (this work) | Experimental vapor at 403 K [13] | Experimental vapor [30] |
|---|---|---|---|
| γ(OH) | 672 | not observed[b] | not reported[c] |
| ν(CC) | 838 | not observed[b] | 847 |
| ν(C–O) | 1164 | 1183 | 1182 |
| b(OH) | 1308 | 1272 | 1264 |
| $\delta_s(CH_3)$ | 1363 | 1385 | 1382 |
| ν(C=O) | 1775 | 1778, 1797[d] | 1788 |
| ν(OH) | 3656 | 3567, 3582, 3595 | 3583 |

[a] γ – out-of-plane bend, ν – stretch, b – in-plane bend, δ – deformation, s – symmetric.
[b] Peaks below 900 $cm^{-1}$ were not observed due to the transparency limit of the $CaF_2$ IR cell windows.
[c] Reported at 650 $cm^{-1}$ in a different publication [31].
[d] The presence of an additional peak is due to acetic acid rotamers [32].

Adsorption of acetic acid ($CH_3COOH$) and its products after breaking the O—H bond – acetate plus a hydrogen atom ($CH_3COO$ + H) – and after breaking the C—OH bond – acetyl plus a hydroxyl group ($CH_3CO$ + OH) – on Pt(111) and Ni(111) were compared in this study with identical computational settings. Our previous studies evaluated the same surface species on Pt(111) and Ni(110) with different computational settings. The current and previous computational settings are compared in Table 4, and the calculated adsorption energies relative to gas-phase acetic acid are listed in Table 5.

On both Pt(111) and Ni(111), molecular acetic acid ($CH_3COOH$) preferentially adsorbs through its carbonyl oxygen to a single metal atom ($\mu_1\eta^1$(O) configuration) with the calculated Pt—O and Ni—O bond distances of 0.22 and 0.20 nm, respectively. The structures are shown with a 3-D view in Fig. 2 and with projection views in Fig. 8a. The calculated adsorption energies were 88 kJ/mol for Pt and 50 kJ/mol for Ni (Table 5). The C=O double bond distance increases slightly from 0.121 nm in gas-phase acetic acid to 0.125 nm in the adsorbed structure on both surfaces.

After breaking the O—H bond, the hydrocarbon fragment, acetate ($CH_3COO$), preferentially forms bidentate species by bonding to two surface metal atoms ($\mu_2\eta^2$(O,O) configuration) on both surfaces (Fig. 8b) with the calculated Pt-O and Ni-O bond distances of 0.21 and 0.20 nm, respectively. A hydrogen atom preferentially adsorbs on a threefold metal site on both surfaces. The calculated dissociative adsorption energies relative to gas-phase acetic acid were 91 kJ/mol for Pt and 124 kJ/mol for Ni (Table 5).

After breaking the C—OH bond, the hydrocarbon fragment, acetyl ($CH_3CO$), preferentially binds to a single Pt atom (atop site) through the C atom that lost the hydroxyl ($\mu_1\eta^1$(C) configuration), and the split-off hydroxyl preferentially binds to a single Pt atom (Fig. 8c). The calculated Pt-O bond distance was 0.301 nm. The calculated dissociative adsorption energies relative to gas-phase acetic acid was 39 kJ/mol (Table 5). On Ni, acetyl in the same $\mu_1\eta^1$(C) configuration has similar dissociative adsorption energy of 35 kJ/mol. However, it is energetically preferable by 16 kJ/mol for acetyl to form an additional bond between the remaining O atom and another Ni atom, binding to a bridge Ni-Ni site

**Table 3**
Experimental IR peaks for acetic acid in a condensed state, $cm^{-1}$.

| Vibration[a] | Multilayer Pt(111), 90 K (this work) | Multilayer Ni(110), 90 K (this work) | Experimental vapor, 298 K [13] | Experimental liquid [33] | Experimental solid [34] |
|---|---|---|---|---|---|
| γ(OH) | 968 | 964 | 948 | 944 | 923 |
| ν(C–O) | 1304 | 1311 | 1294 | 1294 | 1284 |
| ν(C=O) | 1730 | 1730 | 1734 | 1739 | 1648 |
| ν(OH) | 2987 | 2989 | 3030 | 2990 | 2875 |
| ν(CH) | 2930 | 2931 | 2960 | 3030 | – |

[a] γ – out-of-plane bend, ν – stretch.

**Table 4**
Computational settings used in this work and previous studies.

| Surface | Pt(111) | Pt(111) | Ni(111) | Ni(110) |
|---|---|---|---|---|
| Unit cell | 3×3×5 | 3×3×5 | 3×3×5 | 2×4×5 |
| DFT functional | GGA-PBE [4,5] | GGA-PW91 (this work) | GGA-PW91 (this work) | GGA-PW91 [13] |
| basis set | DNP | DNP | DNP | DNP |
| optimized metal lattice constant, nm | 0.3973 (1.2% higher than the experimental value) | 0.3995 (1.8% higher than the experimental value) | 0.3541 (0.5% higher than the experimental value) | 0.3541 (0.5% higher than the experimental value) |
| vacuum spacing | 4 | 4 | 4 | 3 |
| k-point separation, $nm^{-1}$ | 0.4 | 0.4 | 0.4 | 0.4 |
| Monkhorst-Pack grid | 3×3×1 | 3×3×1 | 4×4×1 | 4×2×1 |
| charge and spin density mixing | 0.2 | 0.08 | 0.08 | 0.08 |
| thermal smearing, Ha | 0.002 | 0.002 | 0.002 | 0.002 |
| orbital cutoff distance, nm | 0.45 | 0.4 | 0.4 | 0.4 |
| dispersion correction | Tkatchenko-Scheffler $s_R$ = 0.94 | no | no | no |
| dipole slab correction | yes | no | no | no |

**Table 5**
Calculated energies for acetic acid and its decomposition products on Pt and Ni surfaces relative to gas-phase acetic acid, −ΔE, kJ/mol.

| Surface | Pt(111) | Pt(111) | Ni(111) | Ni(110) |
|---|---|---|---|---|
| Unit cell | 3×3×5 | 3×3×5 | 3×3×5 | 2×4×5 |
| DFT functional | GGA-PBE [4,5] | GGA-PW91 this work | GGA-PW91 this work | GGA-PW91 [13] |
| $CH_3COOH$ | 92 | 88 | 50 | 77 |
| $CH_3COO$ + H | 83 | 91 | 124 | 172 |
| $CH_3CO$ ($\mu_2\eta^2$(C, O)) + OH | Unstable, converts to $\mu_1\eta^1$(C) | Unstable, converts to $\mu_1\eta^1$(C) | 51 | 131 |
| $CH_3CO$ ($\mu_1\eta^1$(C)) + OH | 45 | 39 | 35 | 111 |
| $CH_3C$ + O + OH | −57 | −57 | 90 | Not evaluated |
| $CH_3$ + CO + OH | 79 | 61 | 73 | Not evaluated |

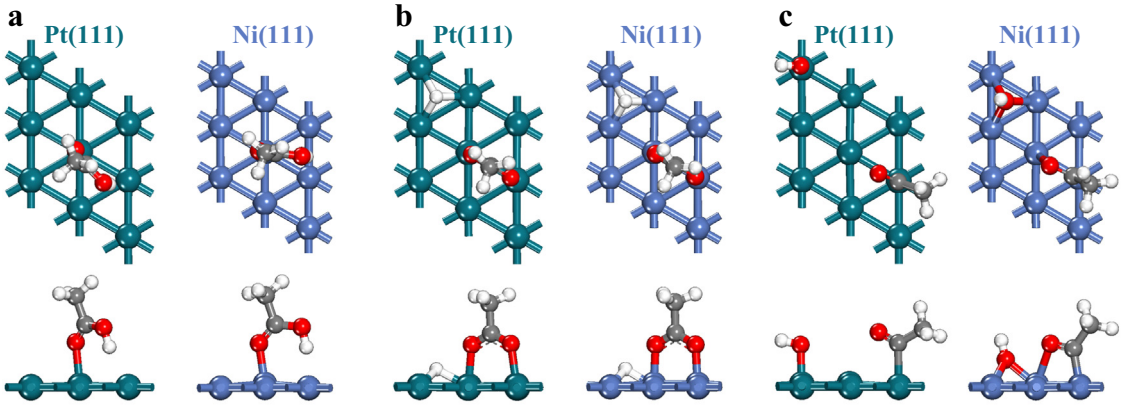


**Fig. 8.** Structures obtained with DFT calculations for adsorption of (a) molecular acetic acid ($CH_3COOH$), (b) acetate and atomic hydrogen ($CH_3COO$ + H) and (c) acetyl and hydroxyl ($CH_3CO$ + OH) on Pt(111) and Ni(111). Side view (upper row) and top view (lower row). Only the top layer of the metal surfaces is shown for clarity.

($\mu_2\eta^2$(C,O) configuration) (Fig. 8c). Hydroxyl on Ni preferentially adsorbs on a threefold site. The calculated C—O bond distances were 0.123 nm for the acetyl binding only through the C atom ($\mu_1\eta^1$(C) configuration) and 0.127 nm for the acetyl binding through both C and O atoms.

**Table 6**
Calculated vibrational frequencies for acetic acid, acetate and acetyl on Pt(111) shown in Fig. 8, $cm^{-1}$.

| Vibration[a] | Acetic acid ($CH_3COOH$) | Acetate ($CH_3COO$) | Acetyl ($CH_3CO$) |
|---|---|---|---|
| ν(CC) | 929 | 981 | 963 |
| ρ($CH_3$) | 1062, 1083 | 1059, 1079 | 1028, 1099 |
| ν(C–O) | 1449 | – | – |
| b(OH) | 1252 | – | – |
| $\delta_s(CH_3)$ | 1411 | 1412 | 1390 |
| $\nu_s(OCO)$ | – | 1425 | – |
| $\delta_a(CH_3)$ | 1498, 1522 | 1489, 1510 | 1480, 1503 |
| $\nu_a(OCO)$ | – | 1564 | – |
| ν(C=O) | 1680 | – | 1781 |
| $\nu_s(CH)$ | 3224 | 3218 | 3186 |
| $\nu_a(CH)$ | 3309, 3353 | 3305, 3336 | 3273, 3305 |
| ν(OH) | 2965 | – | – |

[a] ν – stretch, ρ – rock, b – in-plane bend, δ – deformation, s – symmetric, a – asymmetric.

Frequency calculations for molecular acetic acid, acetate and acetyl on Pt(111) shown in Fig. 8 were performed for the interpretation of the IRAS measurements for acetic acid adsorption on the same surface in Fig. 5a, and the results are provided in Table 6.

For comparing reaction energies for C—O and C—C bond breaking in acetic acid decomposition on Pt(111) and Ni(111), energies for two additional structures were calculated: (1) adsorbed ethylidyne (C—$CH_3$) with atomic oxygen and hydroxyl as well as (2) methyl ($CH_3$) with atomic oxygen and carbon monoxide. The energies relative to gas-phase acetic acid were −57 kJ/mol for ethylidyne on Pt (90 kJ/mol on Ni) and 61 kJ/mol for methyl on Pt (73 kJ/mol on Ni). These values are provided in Table 5 along with our previous results on Pt(111) with different computational settings listed in Table 4. The reaction energies for C—O and C—C bond breaking in acetic acid decomposition on Pt(111) and Ni(111) calculated in this study are illustrated in Fig. 9. The C—OH bond breaking in acetic acid ($CH_3COOH$) with the formation of acetyl ($CH_3CO$) and hydroxyl on Pt was calculated to be endothermic by 49 kJ/mol. In contrast, this reaction was exothermic by 1 kJ/mol on Ni. Even a larger difference was calculated for the C—O bond breaking in acetyl ($CH_3CO$) with the formation of ethylidyne ($CCH_3$) and atomic oxygen. That reaction was endothermic by 96 kJ/mol on Pt and exothermic by 39 kJ/mol on Ni. However, the reactions for the C—C bond breaking in acetyl ($CH_3CO$) with the formation of methyl ($CH_3$) and carbon monoxide (CO) were equally exothermic by 22 kJ/mol on both metals (Fig. 9).

## 4. Discussion

### 4.1. Acetic acid adsorption and surface decomposition

At the employed high exposure conditions of 0.14–0.15 L and the dosing temperature of 90 K in the IRAS spectra in Fig. 5, acetic acid forms a physisorbed multilayer above a single chemisorbed layer on both Pt(111) and Ni(110). The most prominent IRAS peaks at 968, 1304 and 1730 $cm^{-1}$ for Pt in Fig. 5a are consistent with,

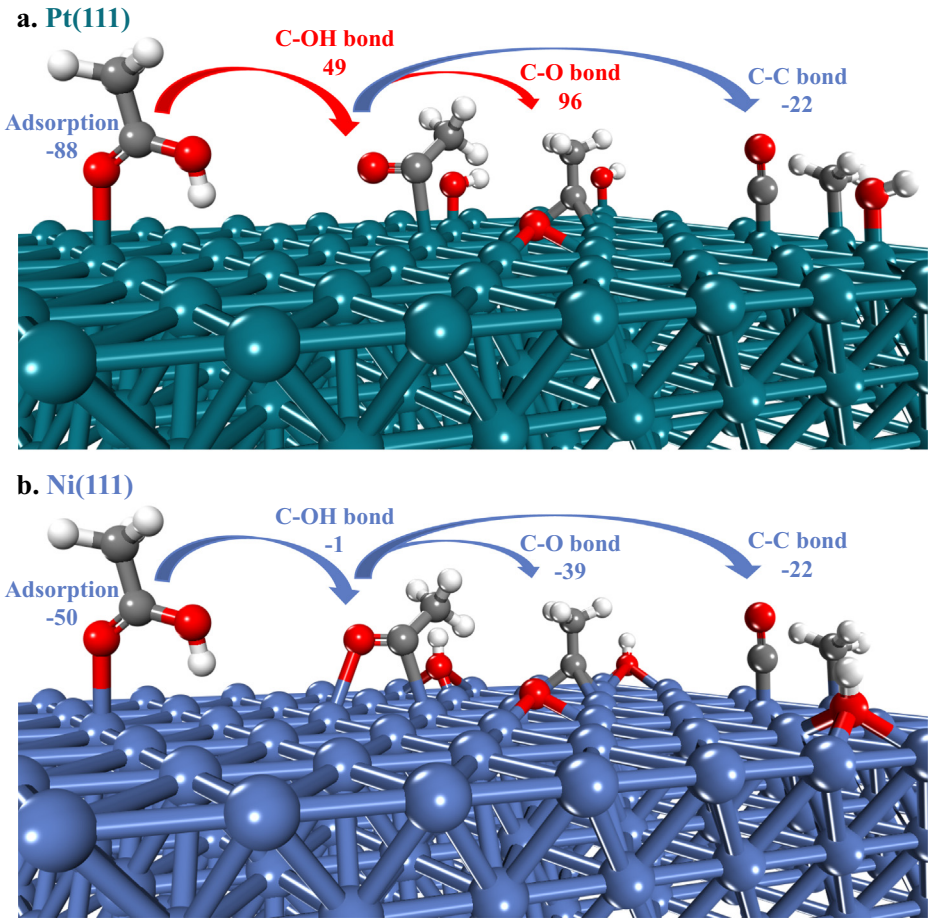


**Fig. 9.** DFT calculated reaction energies on (a) Pt(111) and (b) Ni(111) for acetic acid ($CH_3COOH$) adsorption, C—OH bond breaking in acetic acid with the formation of acetyl and hydroxyl ($CH_3CO$ + OH), C—O bond breaking in acetyl with the formation of ethylidyne and atomic oxygen ($CCH_3$ + O + OH) and C—C bond breaking in acetyl with the formation of methyl and carbon monoxide ($CH_3$ + CO + OH).

respectively, γ(OH), ν(C-O) and ν(C=O) of acetic acid in a condensed state (Table 3). The corresponding IRAS peaks for Ni(110) in Fig. 5b are 964, 1311 and 1730 $cm^{-1}$. The condensed state in this case is a physisorbed multilayer with dimers and catemers, which are various-length chains of more than two hydrogen-bonded acetic acid molecules. The absence of characteristic vibrations for acetic acid monomer (Table 2) demonstrates that at these low-temperature conditions, only dimers and catemers, without any monomers, are present. In particular, the intense ν(OH) peak at 3582 $cm^{-1}$ in the acetic acid vapor-phase spectrum at 403 K reported by us previously [13] (Table 2) is not observed in Fig. 5. Instead, the observed ν(OH) peaks at 2987 $cm^{-1}$ for Pt and 2989 $cm^{-1}$ for Ni are consistent with the presence of dimers and catemers (Table 3).

The peaks at 2930 $cm^{-1}$ for Pt and 2931 $cm^{-1}$ for Ni are due to ν(CH) in both the chemisorbed layer (molecular acetic acid and acetate, Table 6) and the physisorbed multilayer (Table 3). The acetic acid TPD results in Fig. 6a show that the physisorbed multilayer desorbs from the Pt surface at 166 K. This temperature is consistent with 178 K reported previously for acetic acid adsorbed on Pt(111) at 150 K [9]. For Ni, the physisorbed multilayer desorbs in two peaks at 157 and 172 K (Fig. 6b). First, dimers decompose into isolated acetic acid molecules at 157 K. Second, catemers, which have more hydrogen bonds than dimers, decompose into isolated acetic acid molecules at 172 K.

The chemisorbed layer at 90 K on both Pt and Ni contains a mixture of molecularly and dissociatively adsorbed acetic acid. For acetic acid adsorption on Ni(110) at low coverage of 0.18 ML at 90 K, the IRAS peaks at 1065, 1672 and 3017 $cm^{-1}$ were assigned by us to, respectively, ρ($CH_3$), ν(C=O) and ν(OH) of molecularly chemisorbed acetic acid based on our DFT calculations [13]. The similar IRAS peaks at 1055 and 1690 $cm^{-1}$ at a higher coverage of 2.9 ML (exposure of 0.14 L) at 90 K in Fig. 5b, therefore, can also be assigned to, correspondingly, ρ($CH_3$) and ν(C=O) of molecularly adsorbed acetic acid in Fig. 8a.

The IRAS peaks for Ni at 1421 $cm^{-1}$ at 90–350 K and at 1456 $cm^{-1}$ at 90–450 K were assigned by us previously to the $\nu_s$(OCO) vibration of two bridge-bonded bidentate acetate structures: the first bidentate acetate with the lower wavenumber on an unreconstructed Ni(110) surface and the second bidentate acetate on a restructured rough surface [13]. The extent of surface restructuring increases with increasing temperature and acetic acid surface coverage [13]. The same bidentate acetate structure but on Ni(111) instead of Ni(110) is shown in Fig. 8b. The O—H bond breaking in adsorbed acetic acid with the formation of surface acetate and surface hydrogen on Ni at temperatures as low as 90 K is consistent with the first $H_2$ desorption peak at 265 K in the acetic acid TPD in Fig. 7b. This first $H_2$ evolution is desorption limited because it coincides with the $H_2$ desorption from a clean Ni (110) surface [35,36] and, thus, the O—H bond breaking in acetic acid, which generates surface hydrogen, must occur below 265 K.

The peak at 968 $cm^{-1}$ for Pt at 193 K in Fig. 5a is a characteristic out-of-plane bending vibration of the hydroxyl group in adsorbed acetic acid, γ(OH), which was confirmed with a vibrational shift for isotope-substituted acetic acid at 168 K [10]. Since the same peak is observed for Pt in the presence of dimers and catemers at 90 K in Fig. 5a and since it is consistent with similar peaks at 923–948 $cm^{-1}$ in acetic acid condensed states in Table 3, hydroxyl groups of the chemisorbed acetic acid on Pt remain to be affected by hydrogen bonding at 193 K. In contrast, the γ(OH) vibration of an isolated acetic acid molecule unaffected by hydrogen bonding is calculated to be at a much lower wavenumber of 672 $cm^{-1}$ (Table 2), which is in agreement with the experimental peak at 650 $cm^{-1}$ reported for an acetic acid monomer [31].

For Pt at 90 K, the IRAS peaks at 1049 and 1676 $cm^{-1}$ in Fig. 5a are consistent with the calculated vibrational frequencies for molecularly adsorbed acetic acid in Fig. 8a for ρ($CH_3$) at 1062 and 1083 $cm^{-1}$ and for ν(C=O) at 1680 $cm^{-1}$ (Table 6). Similar HREELS peaks with the same assignments were reported for acetic acid adsorption on Pt(111) at 168 K for surface coverage values above 0.5 ML. The peaks were 1034 $cm^{-1}$ for ρ($CH_3$) and 1675 $cm^{-1}$ for ν(C=O) [10]. At surface coverage values below 0.5 ML, primarily acetate was observed instead of molecular acetic acid [10]. The presence of acetate at 90 K in Fig. 5a is evidenced by the peaks at 1412 and 1435 $cm^{-1}$, which are consistent with the calculated $\nu_s$(OCO) at 1425 $cm^{-1}$ for the bridge-bonded bidentate acetate structure (Table 6 and Fig. 8b). A similar peak with the same assignment at 1398 $cm^{-1}$ was reported for acetic acid adsorption on Pt(111) at 163 K [10], at 1427 $cm^{-1}$ for acetic acid adsorption on $Pt/SiO_2$ at 300 K and at 1420 $cm^{-1}$ for acetate adsorption on Pt(100), Pt(110) and Pt(111) in aqueous solution [37]. A mixture of acetic acid and acetate was also detected on Pt (111) at 150 K with SRPES measurements [11]. Similarly to Ni, the first $H_2$ evolution for Pt at 357 K in Fig. 7a is desorption limited because it coincides with the $H_2$ desorption from a clean Pt(111) surface at low $H_2$ coverage [38], providing further evidence for the acetate formation below this temperature.

After the desorption of the physisorbed multilayer, its characteristic vibrations are no longer observed in the IRAS spectra at 193 K for Pt and 200 K for Ni. Specifically, the peaks at 1304, 1730 and 2987 $cm^{-1}$ are no longer observed for Pt in Fig. 5a, and the peaks at 964, 1311, 1730 and 2989 $cm^{-1}$ are no longer observed for Ni in Fig. 5b. The remaining chemisorbed layer on Pt at 193 K contains a mixture of molecularly and dissociatively adsorbed acetic acid. The peaks for molecularly adsorbed acetic acid at 193 K are the same as those at 90 K in Fig. 5a: 968, 1049 and 1676 $cm^{-1}$ for, respectively, γ(OH), ρ($CH_3$) and ν(C=O). The peaks for acetate are shifted to 1406 and 1425 $cm^{-1}$. The appearance of a new small peak at 1703 $cm^{-1}$, which is due to ν(C=O) in acetyl or another decomposition product, indicates the onset of decomposition beyond acetate. For comparison, the calculated ν(C=O) for acetyl in Table 6 is 1781 $cm^{-1}$.

The spectroscopic results in Fig. 5 as well as the computational results in Tables 5 and 6 demonstrate that acetate ($CH_3COO$) preferentially forms bidentate species by bonding through two O atoms to two neighboring surface metal atoms ($\mu_2\eta^2$(O,O) configuration) on both Pt and Ni (Fig. 8b). Contrary to speculations in literature about other possible acetate structures, the bridge-bonded bidentate species in Fig. 8b is the only stable structure. For example, a bridge-bonded monodentate (binding through one O atom to two metal atoms) was found to be metastable on Ni, converting to the more stable bridge-bonded bidentate, and not stable at all on Pt in our DFT calculations. Similarly, an atop-bonded bidentate (binding through two O atoms to a single metal atom) and atop-bonded monodentate (binding through one O atom to a single metal atom) proposed in literature were found to be unstable on both Pt and Ni in our DFT calculations. Moreover, the calculated vibrational frequencies for the bridge-bonded bidentate species on Pt(111) in Table 6 and on Ni(110) reported previously [13] are consistent with the IRAS results in Fig. 5.

At 200 K, acetic acid is more reactive on Ni than on Pt. In contrast with Pt, where a mixture of molecularly adsorbed acetic acid and acetate is observed, most of the chemisorbed acetic acid converts to acetate on Ni. This is evidenced by the disappearance of the IRAS peak at 964 $cm^{-1}$ for γ(OH) at 200 K in Fig. 5b. In addition, the peaks for bridge-bonded bidentate acetates at 1421 and 1456 $cm^{-1}$ become dominant. Furthermore, the appearance of a peak at 1832 $cm^{-1}$ for a bridge-bonded CO [39] indicates the onset of C—C bond breaking reactions below 200 K. The small peak at 2931 $cm^{-1}$ observed at 200 and 350 K is a non-characteristic ν (CH) vibration, which can be due to acetate or another hydrocarbon decomposition product.

The higher reactivity of acetic acid on Ni at 200 K with the formation of acetates and further decomposition with C—C bond breaking prevents its molecular desorption at 220 K. The desorption peak for acetic acid at 220 K is barely visible compared to the peaks for its decomposition products in Fig. 7b. This small desorption peak is more visible as a function of exposure in Fig. 6b. It is followed by a broad tail up to 300 K, which must be due to recombinative desorption through the reaction of a surface acetate with a surface hydrogen atom. In contrast with Ni, most of the chemisorbed acetic acid desorbs from Pt molecularly at 218 K. A similar desorption peak at 223 K for Pt(111) was reported previously [9]. The desorption peak for acetic acid is much larger compared to the peaks for its decomposition products in Fig. 7a. Only at the highest employed exposure of 0.08 L, there is an additional peak at 345 K for recombinative acetic acid desorption in Fig. 6a. The similarity of the acetic acid desorption temperatures of 218 K for Pt(111) and 220 K for Ni(110) demonstrates that the acetic acid adsorption energies on these surfaces are also similar. The similarity of the calculated adsorption energies of 88 kJ/mol for Pt(111) and 77 kJ/mol for Ni(110) in Table 5 is, thus, in agreement with the experimental results.

At 250 K, after the desorption of the chemisorbed acetic acid from Pt at 218 K, only a small amount of acetate and further decomposition products remian on the surface. The IRAS peak at 1406 $cm^{-1}$ at 250 K in Fig. 5a is due to $\nu_s$(OCO) of bridge-bonded bidentate acetate. The peak at 1595 $cm^{-1}$ is likely $\nu$(C=O) of a decomposition product beyond acetyl. The appearance of a peak at 2085 $cm^{-1}$ for atop-bonded (linear) CO [40,41] indicates the onset of C—C bond breaking reactions below 250 K. Correspondingly, the new peak at 974 $cm^{-1}$ is likely due to $CH_x$ species. Based on an analysis of HREELS and TPD results, the presence CH and $CH_2$ rather than $CH_3$ was proposed [9]. At 350 K on Ni, the IRAS peaks for bridge-bonded bidentate acetates at 1421 and 1456 $cm^{-1}$ remain dominant. A new peak at 2010 $cm^{-1}$ for atop-bonded CO in addition to the 1876 $cm^{-1}$ peak for bridge-bonded CO [39] shows further decomposition of the acetates through C—C bond breaking.

By 450 K, the decomposition of acetates is almost complete on both Pt and Ni. On Pt, the only IRAS peaks at 440 K in Fig. 5a are 974 $cm^{-1}$ for $CH_x$ as well as 1878, 2062 and 2085 $cm^{-1}$ for CO. The decomposition of acetates is accompanied by the desorption of $CO_2$ at 388 K, CO at 444 K and $H_2$ at 451 K (Fig. 7a). At 770 K, only peaks at 974 $cm^{-1}$ for $CH_x$ and 2085 $cm^{-1}$ for CO are observed in Fig. 5a. Similarly to Pt, the 1456 $cm^{-1}$ acetate peak becomes small for Ni at 450 K in Fig. 5b. The only other remaining peaks are at 974 $cm^{-1}$ for $CH_x$ and 1055 $cm^{-1}$ for, possibly, $\rho(CH_3)$ in acetate (calculated at 1059 and 1079 $cm^{-1}$, Table 6). The decomposition of acetates on Ni is accompanied by the desorption of $H_2O$ at 310 K and the simultaneous desorption of $H_2$, CO and $CO_2$ at 425 K. The IRAS peaks for CO are no longer observed on Ni at 450 K.

In summary, acetic acid forms similar molecularly adsorbed structures on Pt and Ni (Fig. 8a) with similar adsorption energies (Fig. 6 and Table 5). The structures for acetate and acetyl are also similar (Fig. 8b and c). Acetic acid is more reactive for O—H and C—C bond breaking on Ni below 200 K. Practically all acetic acid decomposes into acetate, and CO is observed on Ni at 200 K whereas on Pt, only a fraction of acetic acid decomposes, and CO is not observed. By 450 K, acetates almost completely decompose, and practically no other oxygen-containing hydrocarbons remain on both Pt and Ni.

### 4.2. Acetic acid hydrodeoxygenation

The IRAS and TPD surface science results in Figs. 5–7 show that acetic acid is equally or even more reactive on Ni compared to Pt. The DFT calculated reaction energies in Fig. 9 are consistent with this conclusion. The C-OH bond breaking in acetic acid with the formation of acetyl ($CH_3CO$), which is usually considered to be rate determining for Pt, [3,5] is endothermic by 49 kJ/mol on Pt (Fig. 9a) but, in contrast, slightly exothermic, −1 kJ/mol, on Ni (Fig. 9b). Similarly, the C-O bond breaking in acetyl ($CH_3CO$) with the formation of ethylidyne ($CCH_3$) is endothermic by 96 kJ/mol on Pt (Fig. 9a) but exothermic by 39 kJ/mol on Ni. The C–C bond breaking reaction in acetyl with the formation of methyl ($CH_3$) and carbon monoxide (CO) is exothermic with similar reaction energies on both Pt and Ni. The results of DFT calculations with transition states for multiple reaction pathways suggested that the rate determining step on Ni may be the formation of acetyl ($CH_3CO$) through the C—O bond breaking in acetate ($CH_3COO$) rather than in acetic acid [3]. However, regardless of the exact reaction mechanism, the surface science results in Figs. 5–7 demonstrate that acetic acid is more reactive on Ni with a greater extent of O—H and C—C bond breaking at 200 K and that all oxygen-containing hydrocarbons almost completely decompose on both Pt and Ni by 450 K.

Acetic acid hydrodeoxygenation is typically performed at or above 450 K. Therefore, acetic acid should be highly reactive at the usual reaction conditions on both Pt and Ni. Moreover, the presence of added $H_2$ under the reaction conditions may further facilitate acetic acid decomposition through hydrogen-assisted C-O bond breaking. Despite the high reactivity of acetic acid on Ni in surface science measurements (Figs. 5–7), the catalytic activity on Ni in reactor testing measurements is low, and it is lower than that on Pt (Fig. 3). These results are consistent with previous studies, in which lower activity of Ni compared to Pt was reported for multiple catalysts and under various reaction conditions. For example, Ni/C was less active than Pt/C in aqueous-phase hydrogenation of acetic acid at 383–482 K [3].

A lower decomposition reactivity of a hydrocarbon under reaction conditions compared to surface science experiments at the same temperature may be caused by the presence of spectator species, which accumulate on the catalytic metal surface during the reaction. Furthermore, carbonaceous species may also accumulate, leading to catalyst deactivation. Since there is no indication in our results that the hydrocarbon surface species on Pt and Ni are considerably different or that Ni deactivates more rapidly than Pt, there must be an additional factor to explain the low catalytic activity of Ni, which is inconsistent with the high reactivity of acetic acid on this metal.

In hydrodeoxygenation, there are two parallel sets of reactions. One set of reactions is for an oxygen-containing hydrocarbon, such as acetic acid. The second set of reactions is for hydrogenation of surface oxygen species with the formation of water. Oxygen species on the catalytic surface are generated through C—O bond breaking. For example, the C—O bond breaking in acetyl ($CH_3CO$) produces ethylidyne ($CCH_3$) and atomic oxygen (Fig. 9). The $H_2$ TPR results in Fig. 4 demonstrate that the reduction of calcined Pt and Ni catalysts takes place at temperatures that are higher than usual hydrodeoxygenation temperatures. The water evolution peak for Pt at 564 K is small because oxygen on Pt nanoparticles is usually limited to the surface and subsurface Pt layers. This temperature is typical for supported Pt nanoparticles, but it can also be as low as 273 K, depending on the catalyst pretreatment and the amount of oxygen [42]. In contrast, the water evolution peak for Ni is large due to bulk oxidation, and it is at a higher temperature of 622 K. This temperature is in agreement with the results of a detailed study on the reduction of a NiO(100) crystal and NiO powders with gas-phase $H_2$ [43]. In a study with Ni nanoparticles with a size from 2 to 22 nm supported on $SiO_2$, the temperature of the water evolution peak in $H_2$ TPR varied between 590 and 683 K, depending on the Ni particle size [1].

Since the surface chemistry of acetic acid on both Pt and Ni is substantially similar, but it is more difficult to reduce Ni than Pt, the lower hydrodeoxygenation activity of Ni can be attributed to its lower reducibility. After acetic acid adsorption, Ni can efficiently catalyze its decomposition reactions below 450 K, but only once. To achieve a catalytic cycle, the Ni surface needs to be reduced by removing surface oxygen species, which requires a significantly higher temperature than that for acetic acid surface reactions. Therefore, the development of improved Ni catalysts with higher activities will benefit by focusing on the reducibility of the metal surface rather than on hydrocarbon reactions.

## 5. Conclusions

The IRAS and TPD measurements show that at high exposure conditions and the dosing temperature of 90 K, acetic acid on Pt (111) and Ni(110) surfaces forms a chemisorbed layer that is covered by a physisorbed multilayer. The physisorbed layer is a condensed state without acetic acid monomers. Instead, it contains dimers and catemers, which are various-length chains of more than two hydrogen-bonded acetic acid molecules. The physisorbed multilayer desorbs from Pt(111) in a single peak at 166 K. For Ni (110), two desorption peaks are observed. Acetic acid dimers decompose into monomers that desorb first at 157 K followed by the decomposition of catemers at 172 K. The chemisorbed layer at 90 K for both Pt and Ni contains a mixture of molecularly adsorbed acetic acid as well as acetate, which is formed through dissociative adsorption by breaking the O—H bond: $CH_3COOH^* + ^* = CH_3COO^* + H^*$.

The DFT calculations show that molecular acetic acid adsorbs similarly on both Pt and Ni surfaces. It preferentially binds through its carbonyl oxygen to a single metal atom ($\mu_1\eta^1$(O) configuration). Acetate ($CH_3COO$) structures are also similar on both surfaces. Acetate preferentially forms bidentate species bonded to two surface metal atoms ($\mu_2\eta^2$(O,O) configuration). The bonding for acetyl ($CH_3CO$), however, is different. On Pt, acetyl preferentially binds to a single surface metal atom through the C atom that lost the hydroxyl ($\mu_1\eta^1$(C) configuration). On Ni, acetyl binds to two surface metal atoms. One metal atom is bonded to the C atom that lost the hydroxyl, and the second metal atom is bonded to the remaining oxygen atom ($\mu_2\eta^2$(C,O) configuration).

The IRAS and TPD measurements show that Ni(110) is more reactive than Pt(111) at 200 K. At this temperature, chemisorbed acetic acid almost completely decomposes into acetate and starts breaking its C—C bond on Ni. In contrast, on Pt, a mixture of molecular acetic acid and acetate is present, and C—C bond breaking is not detected.

Due to the almost complete decomposition of acetic acid to acetate on Ni at 200 K, only a small fraction of the chemisorbed acetic acid desorbs molecularly at 220 K. Although the acetic acid desorption peak for Pt is at a similar temperature of 218 K, most of the chemisorbed acetic acid desorbs from Pt molecularly. Unlike on Ni, only a small fraction of the initial hydrocarbon remains on Pt at higher temperatures. The similarity of the desorption temperatures indicates that the adsorption energies for acetic acid on both metals are also similar. Recombinative desorption of acetic acid, which forms from acetate and hydrogen atoms on the surface, is observed as a small broad peak at 345 K for Pt and as a tail after the 220 K peak, extending to 300 K, for Ni.

The IRAS and TPD measurements at 450 K show that the decomposition of acetic acid is almost complete on both Pt and Ni, with practically no oxygen-containing hydrocarbons remaining on the surface at this temperature. Therefore acetic acid is highly reactive on both Pt and Ni in surface science experiments. However, the Ni/$SiO_2$ catalyst is less active than the Pt/$SiO_2$ catalyst in acetic acid hydrodeoxygenation at 473 and 573 K. This catalytic activity difference cannot be explained by differences in acetic acid adsorption or surface reactivity because they are either similar on Pt and Ni, or Ni is actually more reactive.

The $H_2$ TPR experiments demonstrate that the calcined Pt/$SiO_2$ catalyst is reduced at a lower temperature of 564 K compared to 622 K for the calcined Ni/$SiO_2$ catalyst. Since surface oxygen is produced during hydrodeoxygenation, it needs to be removed by gas-phase $H_2$ to regenerate the metal surface. Such a surface reduction process is parallel with the hydrocarbon decomposition and essential for maintaining the catalytic cycle. Therefore, the lower catalytic activity of Ni can be attributed to its lower reducibility.

These findings will be useful in the development of improved Pt and Ni catalysts for hydrodeoxygenation of biomass-derived feedstocks and other biomass upgrading technologies, such as steam reforming. More broadly, the results will be useful for a wide range of other catalytic technologies that involve reactions of oxygen-containing hydrocarbons on Pt and Ni catalysts.

## Data availability

Data will be made available on request.

## Declaration of Competing Interest

The authors declare that they have no known competing financial interests or personal relationships that could have appeared to influence the work reported in this paper.

## Acknowledgments

This research was supported by the National Science Foundation under Grant CBET-2219872. We thank Dr. Tseng-Ming Chou at Stevens Institute of Technology for help with the TEM measurements and Dr. Emanuel V. Scoullos at Princeton University for the single-crystal experimental measurements. The DFT calculations were performed with the Materials Studio software under a collaborative research Science Ambassador license with Dassault Systèmes BIOVIA Corporation.

## References

[1] F. Yang, D. Liu, Y. Zhao, H. Wang, J. Han, Q. Ge, X. Zhu, Size dependence of vapor phase hydrodeoxygenation of m-cresol on Ni/$SiO_2$ catalysts, ACS Catal. 8 (3) (2018) 1672–1682.
[2] G.W. Huber, S. Iborra, A. Corma, Synthesis of transportation fuels from biomass: chemistry, catalysts, and engineering, Chem. Rev. 106 (9) (2006) 4044–4098.
[3] H. Olcay, L. Xu, Y. Xu, G.W. Huber, Aqueous-phase hydrogenation of acetic acid over transition metal catalysts, ChemCatChem 2 (11) (2010) 1420–1424.
[4] Y. Zheng, Z. Tang, S.G. Podkolzin, Catalytic platinum nanoparticles decorated with subnanometer molybdenum clusters for biomass processing, Chem. - Eur. J. 26 (23) (2020) 5174–5179.
[5] Y. Zheng, Y. Qi, Z. Tang, F. Hanke, S.G. Podkolzin, Kinetics and reaction mechanisms of acetic acid hydrodeoxygenation over Pt and Pt–Mo catalysts, ACS Sustain. Chem. Eng 10 (16) (2022) 5212–5224.
[6] J.M. Crawford, J.B. Jasinski, M.A. Carreon, Towards continuous deoxygenation of acetic acid catalyzed by recyclable mono/bi/trimetallic zeolite catalysts, J. Catal. 401 (2021) 137–148.
[7] K.I. Gursahani, R. Alcalá, R.D. Cortright, J.A. Dumesic, Reaction kinetics measurements and analysis of reaction pathways for conversions of acetic acid, ethanol, and ethyl acetate over silica-supported Pt, Appl. Catal., A 222 (1) (2001) 369–392.
[8] N.R. Avery, Summary abstract: structure and reactivity of carboxylates on Pt (111), J. Vac. Sci. Technol. 20 (3) (1982) 592–593.
[9] Q. Gao, J.C. Hemminger, Chemisorption and thermal decomposition of acetic acid on Pt(111), J. Electron. Spectrosc. Relat. Phenom. 54–55 (1990) 667–676.
[10] Q. Gao, J.C. Hemminger, A vibrational spectroscopy study of $CH_3COOH$, $CH_3COOD$ and $^{13}CD_3COOH$(D) adsorption on Pt(111): I. Surface dimer formation and hydrogen bonding, Surf. Sci. 248 (1) (1991) 45–56.
[11] A. Neitzel, Y. Lykhach, V. Johánek, N. Tsud, T. Skála, K.C. Prince, V. Matolín, J. Libuda, Role of oxygen in acetic acid decomposition on Pt(111), J. Phys. Chem. C 118 (26) (2014) 14316–14325.

[12] W. Rachmady, M.A. Vannice, Acetic acid reduction by $H_2$ over supported Pt catalysts: a DRIFTS and TPD/TPR study, J. Catal. 207 (2) (2002) 317–330.
[13] M.S. Hofman, E.V. Scoullos, J.P. Robbins, L. Ezeonu, D.V. Potapenko, X. Yang, S. G. Podkolzin, B.E. Koel, Acetic acid adsorption and reactions on Ni(110), Langmuir 36 (30) (2020) 8705–8715.
[14] J.P. Robbins, L. Ezeonu, Z. Tang, X. Yang, B.E. Koel, S.G. Podkolzin, Propane dehydrogenation to propylene and propylene adsorption on Ni and Ni-Sn catalysts, ChemCatChem 14 (6) (2022) e202101546.
[15] Y. Zheng, Y. Qi, Z. Tang, J. Tan, B.E. Koel, S.G. Podkolzin, Spectroscopic observation and structure-insensitivity of hydroxyls on gold, Chem. Commun. 58 (25) (2022) 4036–4039.
[16] Y. Zheng, Y. Tang, J.R. Gallagher, J. Gao, J.T. Miller, I.E. Wachs, S.G. Podkolzin, Molybdenum oxide, oxycarbide, and carbide: controlling the dynamic composition, size, and catalytic activity of zeolite-supported nanostructures, J. Phys. Chem. C 123 (36) (2019) 22281–22292.
[17] T. Chen, E. Kertalli, T.A. Nijhuis, S.G. Podkolzin, Effects of hydrogen and propylene presence on decomposition of hydrogen peroxide over palladium catalysts, J. Catal. 341 (2016) 72–81.
[18] J. Gao, Y. Zheng, Y. Tang, J.M. Jehng, R. Grybos, J. Handzlik, I.E. Wachs, S.G. Podkolzin, Spectroscopic and computational study of Cr oxide structures and their anchoring sites on ZSM-5 zeolites, ACS Catal. 5 (5) (2015) 3078–3092.
[19] J. Gao, Y. Zheng, J.M. Jehng, Y. Tang, I.E. Wachs, S.G. Podkolzin, Identification of molybdenum oxide nanostructures on zeolites for natural gas conversion, Science 348 (6235) (2015) 686–690.
[20] J. Gao, Y. Zheng, G.B. Fitzgerald, J. de Joannis, Y. Tang, I.E. Wachs, S.G. Podkolzin, Structure of $Mo_2C_x$ and $Mo_4C_x$ molybdenum carbide nanoparticles and their anchoring sites on ZSM-5 zeolites, J. Phys. Chem. C 118 (9) (2014) 4670–4679.
[21] D.G. Barton, S.G. Podkolzin, Kinetic study of a direct water synthesis over silica-supported gold nanoparticles, J. Phys. Chem. B 109 (6) (2005) 2262–2274.
[22] Z. Tang, T. Chen, K. Liu, H. Du, S.G. Podkolzin, Atomic, molecular and hybrid oxygen structures on silver, Langmuir 37 (39) (2021) 11603–11610.
[23] E.V. Scoullos, M.S. Hofman, Y. Zheng, D.V. Potapenko, Z. Tang, S.G. Podkolzin, B. E. Koel, Guaiacol adsorption and decomposition on platinum, J. Phys. Chem. C 122 (51) (2018) 29180–29189.
[24] K. Liu, T. Chen, S. He, J.P. Robbins, S.G. Podkolzin, F. Tian, Observation and identification of an atomic oxygen structure on catalytic gold nanoparticles, Angew. Chem., Int. Ed. 56 (42) (2017) 12952–12957.
[25] T. Chen, A. Pal, J. Gao, Y. Han, H. Chen, S. Sukhishvili, H. Du, S.G. Podkolzin, Identification of vertical and horizontal configurations for BPE adsorption on silver surfaces, J. Phys. Chem. C 119 (43) (2015) 24475–24488.
[26] J. Gao, H. Zhao, X. Yang, B.E. Koel, S.G. Podkolzin, Geometric requirements for hydrocarbon catalytic sites on platinum surfaces, Angew. Chem., Int. Ed. 53 (14) (2014) 3641–3644.
[27] J. Gao, H. Zhao, X. Yang, B.E. Koel, S.G. Podkolzin, Controlling acetylene adsorption and reactions on Pt–Sn catalytic surfaces, ACS Catal. 3 (6) (2013) 1149–1153.
[28] J. Kim, L.A. Welch, A. Olivas, S.G. Podkolzin, B.E. Koel, Adsorption and decomposition of cyclohexanone (C6H10O) on Pt(111) and the $(2 \times 2)$ and $(\sqrt{3} \times \sqrt{3})$R30°-Sn/Pt(11) surface alloys, Langmuir 26 (21) (2010) 16401–16411.
[29] J. Kim, J. Fu, S.G. Podkolzin, B.E. Koel, Studies of ethylene oxide adsorption on Pt-Sn alloys with TPD, HREELS, UPS, and DFT calculations, J. Phys. Chem. C 114 (40) (2010) 17238–17247.
[30] T. Shimanouchi, Tables of Molecular Vibrational Frequencies, Consolidated Volume I. United States Department of Commerce, U.S. National Bureau of Standards: Washington, D.C., USA, 1972.
[31] M.S. Rosenberg, A.V. Iogansen, A.A. Mashkovsky, S.E. Odinokov, Torsional and librational frequencies of A-H groups as related to H-bonding energies, Spectrosc. Lett. 5 (3–4) (1972) 75–80.
[32] E.M.S. Maçôas, L. Khriachtchev, M. Pettersson, R. Fausto, M. Räsänen, Rotational isomerism in acetic acid: the first experimental observation of the high-energy conformer, J. Am. Chem. Soc. 125 (52) (2003) 16188–16189.
[33] W. Weltner, The vibrational spectrum, associative and thermodynamic properties of acetic acid vapor, J. Am. Chem. Soc. 77 (15) (1955) 3941–3950.
[34] M. Haurie, A. Novak, Spectres de vibration des molecules $CH_3COOH$, $CH_3COOD$, $CD_3COOH$ et $CD_3COOD$—III. Spectres infrarouges des cristaux, Spectrochim. Acta 21 (7) (1965) 1217–1228.
[35] T.E. Jackman, K. Griffiths, W.N. Unertl, J.A. Davies, K.H. Gurtler, D.A. Harrington, P.R. Norton, Surface phases of Ni(110) induced by adsorption of deuterium, Surf. Sci. 179 (2) (1987) 297–321.
[36] K. Christmann, F. Chehab, V. Penka, G. Ertl, Surface reconstruction and surface explosion phenomena in the nickel (110)/hydrogen system, Surf. Sci. 152–153 (1985) 356–366.
[37] A. Rodes, E. Pastor, T. Iwasita, An FTIR study on the adsorption of acetate at the basal planes of platinum single-crystal electrodes, J. Electroanal. Chem. 376 (1) (1994) 109–118.
[38] K. Christmann, G. Ertl, T. Pignet, Adsorption of hydrogen on a Pt(111) surface, Surf. Sci. 54 (2) (1976) 365–392.
[39] B.J. Bandy, M.A. Chesters, P. Hollins, J. Pritchard, N. Sheppard, The chemisorption of carbon monoxide on Ni(110) studied by electron energy loss spectroscopy, J. Mol. Struct. 80 (1982) 203–208.
[40] G. Rupprechter, T. Dellwig, H. Unterhalt, H.J. Freund, High-pressure carbon monoxide adsorption on Pt(111) revisited: a sum frequency generation study, J. Phys. Chem. B 105 (18) (2001) 3797–3802.
[41] S.G. Podkolzin, J. Shen, J.J. de Pablo, J.A. Dumesic, Equilibrated adsorption of CO on silica-supported Pt catalysts, J. Phys. Chem. B 104 (17) (2000) 4169–4180.
[42] T. Huizinga, J. Van Grondelle, R. Prins, A temperature programmed reduction study of Pt on $Al_2O_3$ and $TiO_2$, Appl. Catal. 10 (2) (1984) 199–213.
[43] J.A. Rodriguez, J.C. Hanson, A.I. Frenkel, J.Y. Kim, M. Pérez, Experimental and theoretical studies on the reaction of $H_2$ with NiO: role of o vacancies and mechanism for oxide reduction, J. Am. Chem. Soc. 124 (2) (2002) 346–354.